Optica Applicata, Vol. LV, No. 3, 2025
DOI: 10.37190/oa/207188

High-*Q* silicon microring resonators with optimized spot-size converters

Zhe Han[1,2], Yan Qi[1,*], Yu Wang[1], Yanwei Wang[1], Yuanyuan Fan[1], Boxia Yan[1], Mi Zhou[1], Qian Wang[1], Feifei Gao[3,*]

[1] Institute of Microelectronics of the Chinese Academy of Sciences, Beijing 100029, China

[2] School of Integrated Circuits, University of Chinese Academy of Sciences, Beijing 101408, China

[3] Beijing Specialized Machinery Institute, China Aerospace Science & Industry, Beijing 100143, China

[*]Corresponding authors: qiyan@ime.ac.cn (YQ); gaofeifei16@mails.ucas.ac.cn (FG)

In this paper, an optimized design method for the on-chip microring resonator (MRR) that integrates spot-size converters (SSCs) has been proposed and demonstrated. The tapered SSCs were specially designed based on Bezier free-form curves to improve the quality factor *Q* of the MRRs and reduce their minimum bend radius. Two SSCs with lengths of 25 and 15 μm were designed and employed to construct two MRRs. The two MRRs were subsequently manufactured and experimentally measured. The loaded quality factors of the two MRRs were measured to be 4.34×10^5 and 3.24×10^5, respectively. In comparison to a typical MRR with integrated 50 μm long linear tapered SSCs with the same footprint, the proposed method resulted in a 2.3 and 1.7 times increase in *Q*, as well as a reduction in effective radii from 55 to 25 μm and 15 μm, respectively. This work effectively promotes the improvement of performance and miniaturization of MRRs with integrated SSCs.

Keywords: photonic integrated circuits, microring resonators, Bezier free-form curves.

1. Introduction

In recent years, there has been rapid development in photonic integrated circuits, making it a highly promising technology. A crucial component of PICs is the microring resonator (MRR), which is widely used in various fields, including external cavity lasers [1-3], sensors [4-10], optical communication [11-15], and optical computing [16,17]. To achieve optimal performance, MRRs are typically required to possess a high quality factor *Q* and a large free spectral range (FSR). Additionally, a compact size is essential for enhancing integration.

A lot of methods have been proposed to improve the MRR for high Q and compact size. Some of the approaches focus on improving the manufacturing processes. For instance, the microdisk resonator has been demonstrated as a type of MRR that exhibits both high Q and compact size [18-20]. A microdisk resonator with a radius of 9 μm was measured to have a Q of 9.2×10^5 [18], while another 1-mm-diameter microdisk resonator was reported to achieve a remarkably high Q of 1.94×10^8 [19]. The etchless process is another effective method for increasing the Q of MRRs. This technique utilizes a thermal oxidation process instead of traditional etching methods to generate optical waveguides. By this way, the scattering loss caused by the sidewall roughness of the optical waveguide can be reduced. Researchers have achieved the quality factors as high as 5.1×10^5 [21] and 7.6×10^5 [22] using the etchless process, respectively. Additionally, optimizing the base materials can significantly reduce the loss in optical waveguides, thereby increasing the Q of an MRR. For example, a type of low-loss optical waveguide, consisting of a core and cladding made from differently doped SiO_2, has been used to manufacture MRRs, achieving a Q of 1.83×10^6 [23]. Another study demonstrated a tellurium oxide-clad silicon MRR with a high Q of 1.5×10^6 [24]. However, the aforementioned studies require specific improvements to manufacturing processes or materials, making them incompatible with the CMOS processes and unsuitable for mass production.

There have been studies aimed at improving the Q value of MRRs through design optimization. This approach typically does not require any modifications to the standard processes offered by foundries, making it more conducive to the batch manufacturing of chips and cost reduction. Researchers have identified that the primary cause of optical waveguide loss on chips is the roughness of the sidewalls [25-35]. Increasing the width of the waveguide can improve the Q value by reducing the interaction between the lightwave and the waveguide's sidewalls. However, the conditions for the existence of higher-order modes will be met in wider waveguides, which are referred to as multimode waveguides (MMWs). While the use of MMWs can decrease propagation loss, it may also lead to the excitation of higher-order modes, particularly in bent MMWs. The mode mismatch caused by MMWs can enlarge the loss of the MRR. Therefore, it is crucial to address the mode mismatch issue associated with MMW bends. Some studies suppress the mode mismatch by employing special curves in the design of waveguide bends. For instance, two MRRs with effective radii of 29 and 115 μm were designed using Euler curves, achieving Q values of 1.3×10^6 and 9.4×10^6, respectively [29,34]. However, waveguide bends designed with special curves often possess specific geometries and lack flexibility. A more versatile approach is to utilize narrow single-mode waveguides (SMWs) at the bent sections of the MRR to suppress mode mismatch. Concurrently, spot-size converters (SSCs) are used to connect the bends to the wider MMWs. Using this method, one study achieved a Q value of 2×10^6 under critical coupling [26], while another study obtained a Q value of 1.1×10^6 [27]. However, this method requires very long SSCs to avoid mode mismatches resulting from spot-size conversions. Linear tapered waveguides are the most common type of SSCs.

Linear tapered SSCs with lengths of up to 100 μm were used in references [26] and [28], which severely limited the miniaturization of MRR size and the improvement of the FSR. In this paper, we present a novel type of SSC based on Bezier free-form curves to address this problem. The MRRs with effective radii of 15 and 25 μm are obtained using the proposed method. Their Q values are 3.24×10^5 and 4.34×10^5, respectively. Compared to an MRR with the same footprint that integrates 50 μm long linear tapered SSCs, the proposed method increases the Q by approximately 2.3 and 1.7 times, while reducing their effective radii from 55 to 25 μm and 15 μm, respectively.

2. Design and structure

The SSCs and MRRs were designed based on the standard complementary metal–oxide–semiconductor (CMOS) compatible processes provided by wafer foundries. A silicon-on-insulator (SOI) wafer with a 3 μm SiO_2 buried-oxide (BOX) layer and a 220 nm top silicon layer was utilized as the base material due to its high refractive index difference. To accommodate a wide range of applications, the devices were designed for operation with strip waveguides and the fundamental transverse electric (TE) mode. The three-dimensional (3D) schematic of the SSC, along with the spot-size conversion of the fundamental TE mode, is illustrated in Fig. 1.

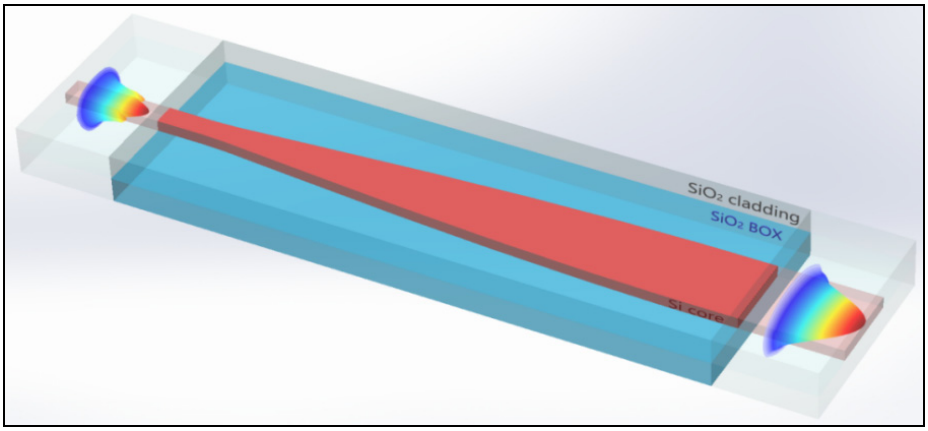

Fig. 1. The 3D view of the designed SSC and the conversion of the fundamental TE mode's spot size.

The Bezier curve is a significant type of mathematical curve that can be used to plot curves with arbitrary changes in curvature. In that sense, the Bezier curve can be regarded as a free-form curve. Consequently, Bezier curves are widely used in fields such as mathematical analysis, computer graphics, and industrial design because of their remarkable flexibility. The continuous nonlinear variation of the curvature and width of on-chip waveguides can be realized by employing Bezier curve in the devices design, which allows for extraordinary performance improvements in devices. In this

paper, Bezier curves are used to design the geometry of SSCs. The path of a Bezier curve is determined by a set of control points, which can be expressed as

$$P(t) = \sum_{k=0}^{n} \binom{n}{k} t^k (1-t)^{n-k} P_k \tag{1}$$

where P_k represents the coordinates of the control points and $P(t)$ denotes the coordinates of the points along the curve. The parameter t is an array that increases from 0 to 1 with each element in t determining the coordinates of a corresponding point on the curve. Consequently, the number of elements in t dictates the number of points that comprise the Bezier curve. The parameter n indicates the order of the Bezier curve and the number of control points is equal to $n+1$. As n increases, the degrees of freedom of the curve also increase, allowing for the design of more complex structures.

For this study, quartic Bezier curves are sufficient to provide the necessary degrees of freedom for the design. The top view of the SSC's geometry, defined by Bezier curves, is shown in Fig. 2. The outline of the Bezier taper consists of two symmetrical curves in the vertical direction, each adjusted by five control points. The coordinates of these control points are determined by several parameters. The parameters L, B_1, B_2, and B_0 are utilized to calculate the x-coordinates of the control points. L represents the total length of the SSC, while B_1, B_2, and B_0 indicate the ratios of the x-coordinates of the corresponding control points to L. Additionally, the parameters W_1, W_2, and W_0 are employed to modify the y-coordinates of the control points and are associated with the widths at various positions of the device. W_1 and W_2 represent the widths of the two ends of the SSC, which correspond to the widths of the SMW and MMW to which the SSC is connected to, respectively. Therefore, the y-coordinates of points P_{u0}, P_{d0}, P_{u4}, and P_{d4} are set to $W_1/2$, $-W_1/2$, $W_2/2$, and $-W_2/2$, respectively. The four points P_{u1}, P_{d1}, P_{u3}, and P_{d3} are strategically placed to facilitate a smoother connection between the SSC and the straight waveguides. The y-coordinates of these four points are set to be the same as those of P_{u0}, P_{d0}, P_{u4}, and P_{d4}, respectively. This alignment ensures that the tangent direction of the Bezier curve at the endpoints is oriented toward the x-axis, which is consistent with the contour lines of the straight waveguides. As a result, this configuration promotes a smoother transition between the SSC and the straight waveguides, enabling more efficient lightwave propagation and thereby reducing losses. Parameters B_1 and B_2 are set to 0.1 and 0.9, respectively, to maintain suitable distances

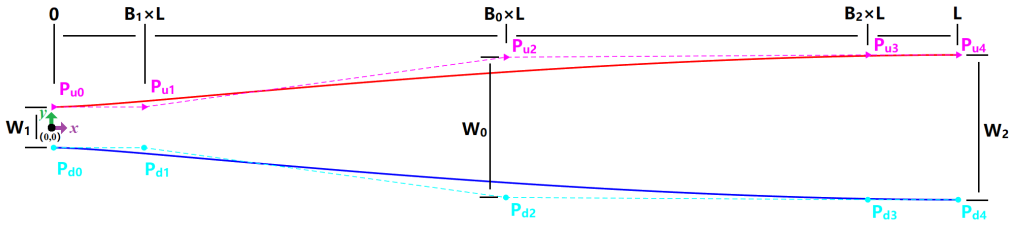

Fig. 2. The structure of the tapered SSC defined by Bezier curves.

for the four points from the two ends of the device along the x-axis. Parameter B_0 is set to 0.5 to position the x-coordinates of P_{u2} and P_{d2} at the midpoint of the device, allowing for adjustments to the overall geometry of the device by varying their y-coordinates. The geometry of the Bezier taper is ultimately defined by the final parameter W_0, with the y-coordinates of P_{u2} and P_{d2} set to $W_0/2$, and $-W_0/2$, respectively.

Here, we summarize the coordinates of all the ten control points as follows:

$$P_{u0}\left[0, \frac{w_1}{2}\right],\ P_{u1}\left[B_1 \times L, \frac{w_1}{2}\right],\ P_{u2}\left[B_0 \times L, \frac{w_0}{2}\right],\ P_{u3}\left[B_2 \times L, \frac{w_2}{2}\right],\ P_{u4}\left[L, \frac{w_2}{2}\right]$$

$$P_{d0}\left[0, -\frac{w_1}{2}\right],\ P_{d1}\left[B_1 \times L, -\frac{w_1}{2}\right],\ P_{d2}\left[B_0 \times L, -\frac{w_0}{2}\right],\ P_{d3}\left[B_2 \times L, -\frac{w_2}{2}\right],$$

$$P_{d4}\left[L, -\frac{w_2}{2}\right]$$

Using our proposed method, we designed two SSCs with waveguide width conversions of 0.45 to 2.5 μm and 0.45 to 1.6 μm, respectively. The width of the SMW (W_1) was set to 0.45 μm due to its excellent single-mode maintenance properties. The widths of the MMWs (W_2) were set to 2.5 and 1.6 μm, respectively, in order to demonstrate the effectiveness of our method. We used a finite-difference time-domain (FDTD) algorithm with non-uniform grid sizes provided by commercial software Lumerical to simulate the optical transmission in the devices and evaluate their performance. The mesh accuracy was set to level 6 to achieve high-precision simulation results. The operation wavelength was chosen as 1550 nm. The refractive index data for the materials were directly sourced from the software database. A fundamental TE mode source was launched at the SMW port, and its output at the MMW port was observed after propagating through the device. Monitors were placed at the MMW port to detect the device's transmission and the excitation of high-order modes within the device. Based on our evaluation, we determined the optimal lengths (L) of the two SSCs to be 20 and 10 μm, respectively. The lengths were determined based on the shortest lengths of the SSCs designed using our method, while ensuring their performance. The optimal structure of the device was achieved by adjusting the parameter W_0. As an example, Fig. 3(a) shows how the fundamental mode transmission of the 0.45 to 1.6 μm Bezier tapered SSC varies with the parameter W_0. It can be seen that the highest transmission of the fundamental mode occurs when W_0 is equal to 1.55 μm. Therefore, the device structure determined by W_0 = 1.55 μm is optimal. We also calculated the fundamental mode transmission of the device across the entire C-band. For comparison, we calculated the fundamental mode transmissions of 0.45 to 1.6 μm linear tapered SSCs with lengths of 10 and 50 μm. The results are shown in Fig. 3(b). It is evident that the performance of the designed Bezier tapered SSC is significantly better than that of the linear tapered SSC with a length of 10 μm, and is comparable to that of the linear taper with a length of 50 μm. Considering the error of simulation results and in order to be more intuitive, Fig. 3(a) and (b) compare the simulation results using relative values. The 20 μm long

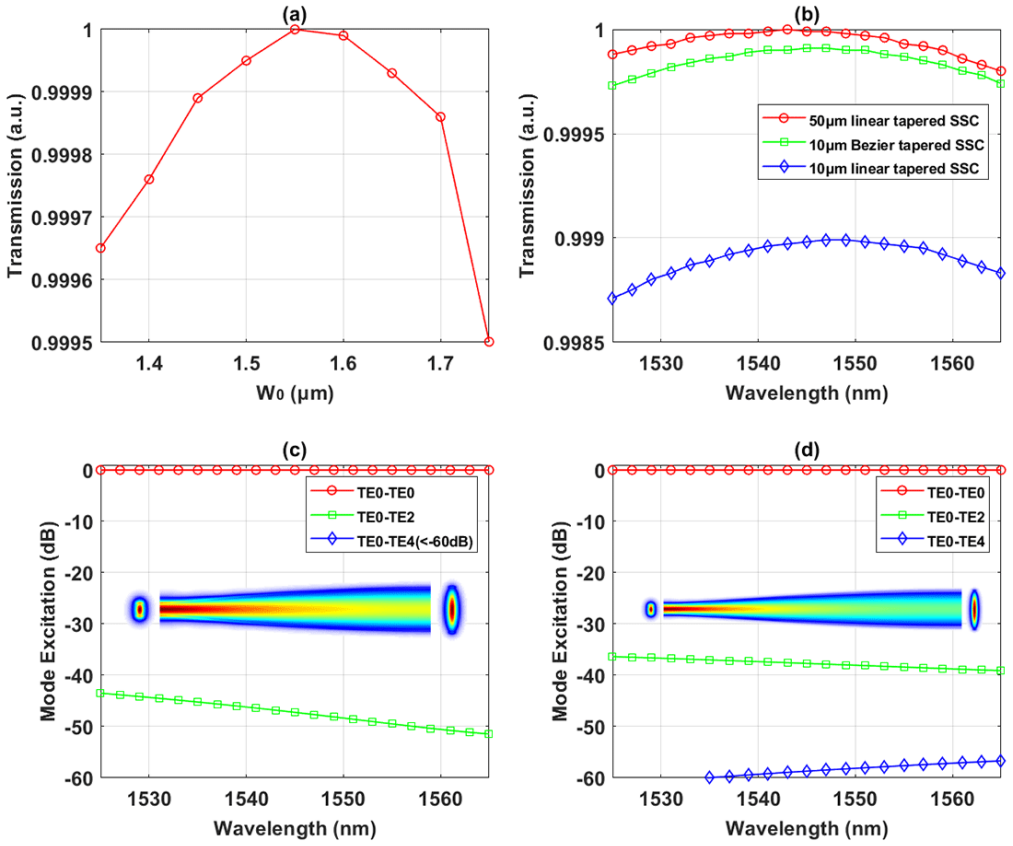

Fig. 3. (a) The fundamental mode transmission of the 0.45 to 1.6 μm Bezier tapered SSC varies with the parameter W_0. (b) The comparison of the fundamental mode transmission between the Bezier and linear tapered SSCs within the C-band range. The mode excitation of the (c) 0.45 to 1.6 μm and (d) 0.45 to 2.5 μm Bezier tapered SSC during spot-size conversion within the C-band range. The insets show the field distributions of the input and output of the fundamental mode, and a top view of the beam propagation in the SSCs.

0.45 to 2.5 μm Bezier tapered SSC was designed using the same method, and its W_0 was determined to be 2.54. Figures 3(c) and (d) illustrate the mode excitation caused by the two Bezier tapered SSCs within the C-band range during the spot-size conversion, respectively. Due to the symmetry of the device structure, symmetric modes are more easily excited. It can be observed that the excitation of high-order modes in the 0.45 to 1.6 μm and 0.45 to 2.5 μm Bezier tapered SSC remains below –40 dB and –30 dB, respectively. The insets show the field distributions of the input and output of the fundamental mode, as well as a top view of the beam propagation in the SSCs. It is evident that the fundamental mode is well maintained while propagating through the designed devices.

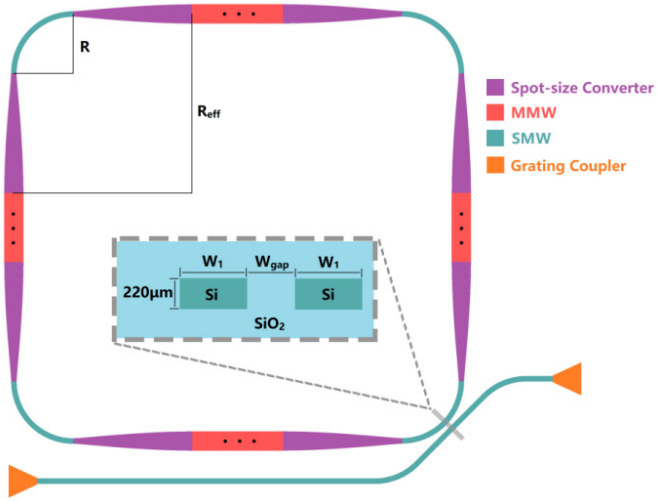

Fig. 4. The top view of the designed MRR. The inset shows the cross-section of the waveguides at the light coupling position.

We utilized the specially designed SSCs to construct MRRs, as depicted in Fig. 4. For comparison, we also constructed an MRR with 50 μm long 0.45 to 1.6 μm linear tapered SSCs. The MRRs consist of bent SMWs, straight MMWs, tapered SSCs, and a directional coupler. A 0.45 μm wide waveguide arc with a radius R of 5 μm is used as the single-mode waveguide bend. The effective radius R_{eff} is defined as the minimum bending radius of the ring, which, in this case, is the sum of the radius of the waveguide arc and the length of the SSC. Therefore, the effective radii of the three MRRs are 25, 15, and 55 μm, respectively. The MMWs, with widths of 1.6 and 2.5 μm, were selected to match the SSCs. All three MRRs were adjusted to maintain the same circumference of 743.4 μm by altering the lengths of the MMWs. The inset in Fig. 4 illustrates the cross-section of the directional coupler, which comprises a SMW arc and an adjacent straight SMW. Both have a width of W_1, and the spacing (W_{gap}) between them can be adjusted to control the transmission of the directional coupler. Here, W_{gap} was set to 0.265 μm to achieve a transmission of approximately 0.6%, allowing the MRRs to operate in an undercoupled state. Vertical grating couplers were used to realize the optical coupling between the devices and optical fiber pigtails.

3. Fabrication and measurement

The designed MRRs were fabricated using the multi-project wafer (MPW) service provided by the Institute of Microelectronics of Chinese Academy of Sciences. This MPW service offers CMOS-compatible photonic chip manufacturing processes based on standard SOI wafers with a 3 μm BOX and 220 nm top silicon. The vertical grating couplers were selected from the device library provided by the foundry, while the re-

maining parts of the MRRs were constructed entirely from strip waveguides, requiring only a full etching process.

A system was established for device testing, including a light source, an optical power meter, and other equipment. A C-band tunable laser (Thorlabs TLX1) served as the light source and was connected to the device's input port. An optical power meter (Newport 918D) was used to measure the optical power at the device's output port. The light beam was transmitted between the chip and the light source and detector using polarization-maintaining fibers, and they were aligned with high-precision optical stages. The Q values and FSRs of the three MRRs were measured near the wavelength of 1550 nm using the testing system, with the results presented in Fig. 5. The data for the resonant peaks shown in the figure represent the best results obtained from multiple measurements. The FWHM of the resonance curve was determined by fitting the test data to a Lorentzian curve. The FWHMs of the MRRs with 0.45 to 2.5 μm Bezier tapered SSCs, 0.45 to 1.6 μm Bezier tapered SSCs, and 0.45 to 1.6 μm linear tapered SSCs were measured to be 3.57, 4.79, and 8.18 pm, respectively. Their loaded quality factors were calculated using the formula $Q_{\text{load}} = \lambda / \text{FWHM}$, resulting in values of 4.34×10^5, 3.24×10^5 and 1.89×10^5, respectively. Since all three MRRs have the same circumference, their measured FSRs were all around 0.85 nm. It should be noted

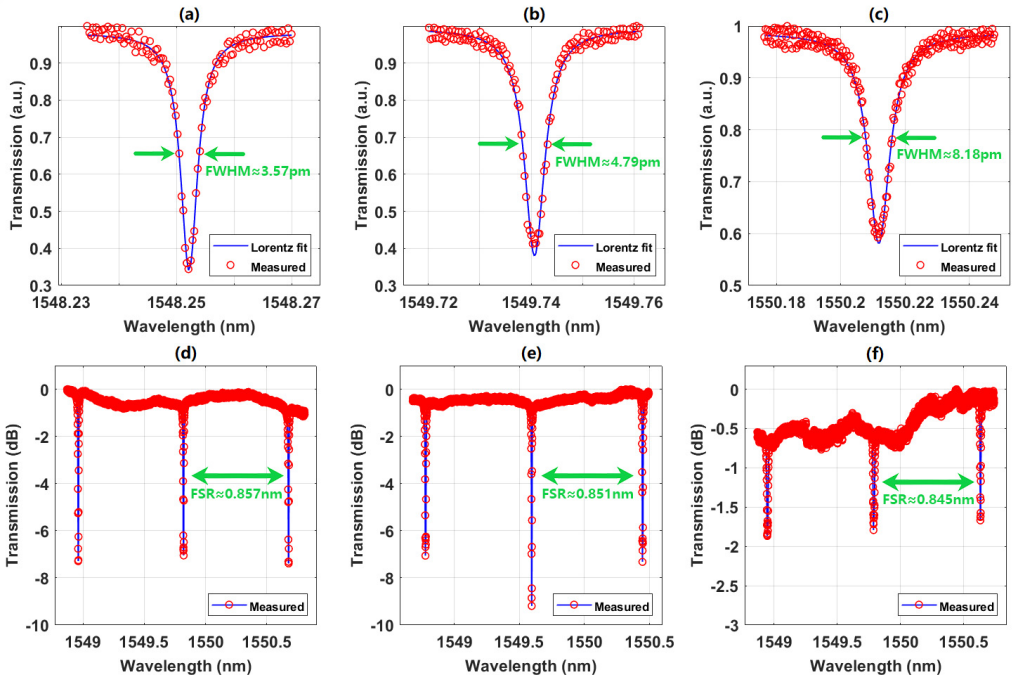

Fig. 5. The measured resonance peaks and their fitted Lorentzian curves of the MRRs with (a) 0.45 to 2.5 μm Bezier tapered SSCs, (b) 0.45 to 1.6 μm Bezier tapered SSCs, and (c) 0.45 to 1.6 μm linear tapered SSCs. The measured FSRs of the MRRs with (d) 0.45 to 2.5 μm Bezier tapered SSCs, (e) 0.45 to 1.6 μm Bezier tapered SSCs, and (f) 0.45 to 1.6 μm linear tapered SSCs.

that the resonance depth of the MRRs designed using this method was greater than that of the MRRs with linear tapered SCCs under the same operating conditions, further demonstrating the effectiveness of this method in reducing MRR loss.

4. Conclusion

In this paper, we propose a design method for SSCs based on Bezier free-form curves and apply the designed SSCs to MRRs. Our method results in significantly more compact SSCs compared to conventional linear tapered SSCs. This advancement also leads to a reduction in the effective radius of MRRs. Specifically, our method reduces the effective radii of MRRs from 55 to 25 μm and 15 μm, while simultaneously increasing their *Q* factors by 2.3 and 1.7 times, respectively. This method has greatly advanced the performance improvement of the high-*Q* MRRs with integrated SSCs, enhancing their applicability across various fields.

Funding
This work was supported by National Key Research and Development Program of China (2023YFB3610901); National Natural Science Foundation of China (12074405); Youth Innovation Promotion Association, CAS (2020121).

References

[1] Fang Z., Chen Q.Y., Zhao C.Z., *A review of recent progress in lasers on silicon*, Optics & Laser Technology **46**, 2013: 103-110. https://doi.org/10.1016/j.optlastec.2012.05.041

[2] Xiang C., Jin W., Guo J., Williams C., Netherton A.M., Chang L., Morton P.A., Bowers J.E., *Effects of nonlinear loss in high-Q Si ring resonators for narrow-linewidth III-V/Si heterogeneously integrated tunable lasers*, Optics Express **28**(14), 2020: 19926-19936. https://doi.org/10.1364/OE.394491

[3] Aihara T., Hiraki T., Fujii T., Takeda K., Tsuchizawa T., Kakitsuka T., Fukuda H., Matsuo S., *Heterogeneously integrated widely tunable laser using lattice filter and ring resonator on Si photonics platform*, Optics Express **30**(10), 2022: 15820-15829. https://doi.org/10.1364/OE.448059

[4] Makela M., Lin Z., Coté G.L., Lin P.T., *Fluorescence enhanced biomolecule detection using direct laser written micro-ring resonators*, Optics & Laser Technology **174**, 2024: 110629. https://doi.org/10.1016/j.optlastec.2024.110629

[5] Ciminelli C., Dell'Olio F., Conteduca D., Campanella C.M., Armenise M.N., *High performance SOI microring resonator for biochemical sensing*, Optics & Laser Technology **59**, 2014: 60-67. https://doi.org/10.1016/j.optlastec.2013.12.011

[6] Samanta S., Kalathimekkad S., Selvaraja S.K., *Fluid sensing strategies adopted in photonic devices: A review*, Optics & Laser Technology **139**, 2021: 106975. https://doi.org/10.1016/j.optlastec.2021.106975

[7] De Carlo M., De Leonardis F., Lamberti L., Passaro V.M.N., *Design of a resonator-bus-resonator anti-parity-time-symmetric integrated optical gyroscope*, Optics and Lasers in Engineering **153**, 2022: 106983. https://doi.org/10.1016/j.optlaseng.2022.106983

[8] Su B., Wang C., Kan Q., Chen H., *Compact silicon-on-insulator dual-microring resonator optimized for sensing*, Journal of Lightwave Technology **29**(10), 2011: 1535-1541. https://doi.org/10.1109/JLT.2011.2138678

[9] Guillén-Torres M.A., Cretu E., Jaeger N.A.F., Chrostowski L., *Ring resonator optical gyroscopes—Parameter optimization and robustness analysis*, Journal of Lightwave Technology **30**(12), 2012: 1802-1817. https://doi.org/10.1109/JLT.2012.2188884

[10] DAI D., HE S., *Highly sensitive sensor based on an ultra-high-Q Mach–Zehnder interferometer-coupled microring*, Journal of the Optical Society of America B **26**(3), 2009: 511-516. https://doi.org/10.1364/JOSAB.26.000511
[11] CHEN J., GAO D., *A silicon-based compact triplexer using Bragg grating assisted non-reciprocal single microring resonator*, Optics & Laser Technology **124**, 2020: 105971. https://doi.org/10.1016/j.optlastec.2019.105971
[12] RASRAS M.S., TU K.Y., GILL D.M., CHEN Y.K., WHITE A.E., PATEL S.S., POMERENE A., CAROTHERS D., BEATTIE J., BEALS M., MICHEL J., KIMERLING L.C., *Demonstration of a tunable microwave-photonic notch filter using low-loss silicon ring resonators*, Journal of Lightwave Technology **27**(12), 2009: 2105-2110. https://doi.org/10.1109/JLT.2008.2007748
[13] LIU D., XU H., TAN Y., SHI Y., DAI D., *Silicon photonic filters*, Microwave and Optical Technology Letters **63**(9), 2021: 2252 - 2268. https://doi.org/10.1002/mop.32509
[14] XIE Y., SHI Y., LIU L., WANG J., PRITI R., ZHANG G., LIBOIRON-LADOUCEUR O., DAI D., *Thermally -reconfigurable silicon photonic devices and circuits*, IEEE Journal of Selected Topics in Quantum Electronics **26**(5), 2020: 3600220. https://doi.org/10.1109/JSTQE.2020.3002758
[15] YANG H., LI J., HU G., YUN B., CUI Y., *Hundred megahertz microwave photonic filter based on a high Q silicon nitride multimode microring resonator*, OSA Continuum **3**(6), 2020: 1445-1455. https://doi.org/10.1364/OSAC.392053
[16] CAI L., LU Y., ZHU H., *Performance enhancement of on-chip optical switch and memory using $Ge_2Sb_2Te_5$ slot-assisted microring resonator*, Optics and Lasers in Engineering **162**, 2023: 107436. https://doi.org/10.1016/j.optlaseng.2022.107436
[17] XIA Y., ZHOU S., CHEN F., YU X., LIU J., LI F., SUI X., *A multifunctional optical computing system based on directed logic and micro-ring resonator*, Optics & Laser Technology **175**, 2024: 110696. https://doi.org/10.1016/j.optlastec.2024.110696
[18] JIANG W.C., ZHANG J., LIN Q., *Compact suspended silicon microring resonators with ultrahigh quality*, Optics Express **22**(1), 2014: 1187-1192. https://doi.org/10.1364/OE.22.001187
[19] GU J., LIU J., BAI Z., WANG H., CHENG X., LI G., ZHANG M., LI X., SHI Q., XIAO M., JIANG X., *Dry -etched ultrahigh-Q silica microdisk resonators on a silicon chip*, Photonics Research **9**(5), 2021: 722-725. https://doi.org/10.1364/PRJ.412840
[20] LIU S., SUN W., WANG Y., YU X., XU K., HUANG Y., XIAO S., SONG Q., *End-fire injection of light into high-Q silicon microdisks*, Optica **5**(5), 2018: 612-616. https://doi.org/10.1364/OPTICA.5.000612
[21] LUO L.W., WIEDERHECKER G.S., CARDENAS J., POITRAS C., LIPSON M., *High quality factor etchless silicon photonic ring resonators*, Optics Express **19**(7), 2011: 6284-6289. https://doi.org/10.1364/OE.19.006284
[22] GRIFFITH A., CARDENAS J., POITRAS C.B., LIPSON M., *High quality factor and high confinement silicon resonators using etchless process*, Optics Express **20**(19), 2012: 21341-21345. https://doi.org/10.1364/OE.20.021341
[23] YIN Y.-X., YIN X.-J., ZHANG X.-P., YAN G.-W., WANG Y., WU Y.-D., AN J.-M., WANG L.-L., ZHANG D.-M., *High-Q-factor silica-based racetrack microring resonators*, Photonics **8**(2), 2021: 43. https://doi.org/10.3390/photonics8020043
[24] MIARABBAS KIANI K., BONNEVILLE D.B., KNIGHTS A.P., BRADLEY J.D.B., *High-Q TeO_2–Si hybrid microring resonators*, Applied Sciences **12**(3), 2022: 1363. https://doi.org/10.3390/app12031363
[25] JI X., BARBOSA F.A.S., ROBERTS S.P., DUTT A., CARDENAS J., OKAWACHI Y., BRYANT A., GAETA A.L., LIPSON M., *Ultra-low-loss on-chip resonators with sub-milliwatt parametric oscillation threshold*, Optica **4**(6), 2017: 619-624. https://doi.org/10.1364/OPTICA.4.000619
[26] GUILLÉN-TORRES M.A., MURRAY K., YUN H., CAVERLEY M., CRETU E., CHROSTOWSKI L., JAEGER N.A.F., *Effects of backscattering in high-Q, large-area silicon-on-insulator ring resonators*, Optics Letters **41**(7), 2016: 1538-1541. https://doi.org/10.1364/OL.41.001538

[27] Zhang Y., Hu X., Chen D., Wang L., Li M., Feng P., Xiao X., Yu S., *Design and demonstration of ultra-high-Q silicon microring resonator based on a multi-mode ridge waveguide*, Optics Letters **43**(7), 2018: 1586–1589. https://doi.org/10.1364/OL.43.001586

[28] Mou B., Boxia Y., Yan Q., Yanwei W., Zhe H., Fan Y., Yu W., *Ultrahigh Q SOI ring resonator with a strip waveguide*, Optics Communications **505**, 2022: 127437. https://doi.org/10.1016/j.optcom.2021.127437

[29] Zhang L., Jie L., Zhang M., Wang Y., Xie Y., Shi Y., Dai D., *Ultrahigh-Q silicon racetrack resonators*, Photonics Research **8**(5), 2020: 684-689. https://doi.org/10.1364/PRJ.387816

[30] Yap K.P., Delage A., Lapointe J., Lamontagne B., Schmid J.H., Waldron P., Syrett B.A., Janz S., *Correlation of scattering loss, sidewall roughness and waveguide width in silicon-on-insulator (SOI) ridge waveguides*, Journal of Lightwave Technology **27**(18), 2009: 3999-4008. https://doi.org/10.1109/JLT.2009.2021562

[31] Lee K.K., Lim D.R., Luan H.-C., Agarwal A., Foresi J., Kimerling L.C., *Effect of size and roughness on light transmission in a Si/SiO$_2$ waveguide: Experiments and model*, Applied Physics Letters **77**(11), 2000: 1617-1619. https://doi.org/10.1063/1.1308532

[32] Shang H., Sun D., Yu P., Wang B., Yu T., Li T., Jiang H., *Investigation for sidewall roughness caused optical scattering loss of silicon-on-insulator waveguides with confocal laser scanning microscopy*, Coatings **10**(3), 2020: 236. https://doi.org/10.3390/coatings10030236

[33] Hagan D.E., Knights A.P., *Mechanisms for optical loss in SOI waveguides for mid-infrared wavelengths around 2 μm*, Journal of Optics **19**(2), 2017: 025801. https://doi.org/10.1088/2040-8986/19/2/025801

[34] Zhang L., Hong S., Wang Y., Yan H., Xie Y., Chen T., Zhang M., Yu Z., Shi Y., Liu L., Dai D., *Ultralow-loss silicon photonics beyond the singlemode regime*, Laser & Photonics Reviews **16**(4), 2022: 2100292. https://doi.org/10.1002/lpor.202100292

[35] Bauters J.F., Heck M.J.R., John D., Dai D., Tien M.C., Barton J.S., Leinse A., Heideman R.G., Blumenthal D.J., Bowers J.E., *Ultra-low-loss high-aspect-ratio Si$_3$N$_4$ waveguides*, Optics Express **19**(4), 2011: 3163-3174. https://doi.org/10.1364/OE.19.003163

Received January 6, 2025
in revised form May 20, 2025